NANO · MICRO small
www.small-journal.com

High Cathode Loading and Low-Temperature Operating Garnet-Based All-Solid-State Lithium Batteries – Material/Process/Architecture Optimization and Understanding of Cell Failure

Hirotoshi Yamada, Tomoko Ito, Tatsuya Nakamura, Raman Bekarevich, Kazutaka Mitsuishi, Sanoop Palakkathodi Kammampata, and Venkataraman Thangadurai**

All-solid-state lithium batteries (ASSLBs) are prepared using garnet-type solid electrolytes by quick liquid phase sintering (Q-LPS) without applying high pressure during the sintering. The cathode layers are quickly sintered with a heating rate of 50–100 K min^{-1} and a dwell time of 10 min. The battery performance is dramatically improved by simultaneously optimizing materials, processes, and architectures, and the initial discharge capacity of the cell with a $LiCoO_2$-loading of 8.1 mg reaches 1 mAh cm^{-2} and 130 mAh g^{-1} at 25 °C. The all-solid-state cell exhibits capacity at a reduced temperature (10 °C) or a relatively high rate (0.1 C) compared to the previous reports. The Q-LPS would be suitable for large-scale manufacturing of ASSLBs. The multiphysics analyses indicate that the internal stress reaches 1 GPa during charge/discharge, which would induce several mechanical failures of the cells: broken electron networks, broken ion networks, separation of interfaces, and delamination of layers. The experimental results also support these failures.

1. Introduction

High-performance secondary batteries are important for zero-emission societies. Among several secondary batteries, lithium-ion batteries (LIBs) are widely used in many applications from portable electronic devices to electric vehicles. However, in the automotive industry, internal combustion engines using fossil fuels are still superior to LIBs in terms of energy density, charge time, cost, reliability (cycle life and calendar life), and safety. Ceramic all-solid-state batteries (ASSBs) are one of the candidates for next-generation batteries because of their potential high energy density and high safety.[1,2] These advantages of ceramic ASSBs are due to the physicochemical properties of ceramic solid electrolytes (CSEs). Some CSEs show high electrochemical stability that can be used with high-voltage cathode materials above 4.5 V versus Li/Li^+ and/or lithium metal anode.[3–5] Lithium metal is the ultimate anode with its lowest electrode potential and the largest specific capacity. Among several CSEs, garnet-type $Li_7La_3Zr_2O_{12}$ (LLZ) and its related phases have attracted keen interest because of their high ionic conductivity (≈10^{-3} S cm^{-1} at room temperature) and their electrochemical

H. Yamada, T. Ito
Graduate School of Engineering
Nagasaki University
Nagasaki 852-8521, Japan
E-mail: h-yama@nagasaki-u.ac.jp

The ORCID identification number(s) for the author(s) of this article can be found under https://doi.org/10.1002/smll.202301904.

[+]Present address: Advanced Microscopy Laboratory, The Centre for Research on Adaptive Nanostructures and Nanodevices (CRANN), Trinity College Dublin, Dublin, D02 DA31, Ireland

T. Nakamura
Graduate School of Engineering
University of Hyogo
Himeji, Hyogo 671-2280, Japan

R. Bekarevich,[+] K. Mitsuishi
Research Center for Advanced Measurement and Characterization
National Institute for Materials Science
Tsukuba 305-0047, Japan

S. P. Kammampata, V. Thangadurai
Department of Chemistry
University of Calgary
Calgary, Alberta T2N 1N4, Canada
E-mail: vthangad@ucalgary.ca

DOI: 10.1002/smll.202301904

stability with lithium metal.[5–7] These attractive properties have impacted studies toward garnet-based all-solid-state lithium batteries (ASSLBs). Since its first report, much attention has been paid to lithium anode toward the high-energy-density lithium metal batteries: area-specific resistance of lithium plating/stripping[8–12] and short circuits resulting from lithium penetration through the solid electrolyte layers.[9,11–26]

On the cathode side, a small portion of organic or polymer electrolyte is generally added to promote ion transfer in the cathode layers.[2] Fewer studies have been reported on all ceramic cathode layers, mainly due to the difficulty of co-sintering of cathode layers. As the typical sintering temperature of LLZ is so high as 1100 °C or even higher, it is challenging to prepare the dense interface between conventional active materials ($LiCoO_2$ (LCO), $LiNi_{1-x-y}Co_xMn_yO_2$ (NCM), $LiFePO_4$) and LLZ. In general, a single-phase ceramic material is sintered at high temperatures and/or high pressure. However, for heterogeneous systems, such as composites of active materials and solid electrolytes, high-temperature processes would result in the interdiffusion of each element to form interphases between two materials,[27] which would cause low electrochemical activity of those materials and high electrical resistance. For LLZ, it is reported that co-sintering with LCO results in interphases like La_2CoO_4 or $LaCoO_3$.[28,29] Ohta et al. employed Li_3BO_3 or $Li_{3-x}C_xB_{1-x}O_3$ (LCBO) as a solid electrolyte in the cathode layer, which exhibits a relatively low melting point of 700 °C.[30] When the mixed powder consisting of Li_3BO_3 and LCO is coated on an LLZ pellet and is heated above 700 °C, molten Li_3BO_3 or LCBO fills voids among LCO particles, and after cooling, both the ion network and the dense interface in the cathode layer are formed. The obtained cell Li | LLZ | LCBO | LCO exhibited an initial discharge capacity of 85 mAh g^{-1} at room temperature. The drawback of this method is the low ionic conductivity of LCBO (≈10^{-6} S cm^{-1}),[31] which causes high resistance in the cathode composite. Han et al. prepared a cathode layer consisting of LCO, LLZ, and LCBO, in which LCO and LLZ particles are embedded in an LCBO matrix.[32] Although the cell exhibited a higher initial discharge capacity of 92 mAh g^{-1} at 0.05C, the loading of LCO was as low as 1 mg cm^{-2}. In the series connection of the high ionic conductor (LLZ; 10^{-3}–10^{-4} S cm^{-1}) and the low ionic conductor (LCBO; ≈10^{-6} S cm^{-1}), the total conductivity is dominated by the latter. Therefore, it is essential to ensure the formation of direct contact between LLZ and active materials.

Guillon and his co-workers systematically studied the composite cathode layers using LCO and LLZ without low-melting-point (and low-conductive) ionic conductors.[33–35] According to Uhlenbruck et al., thermal reactions between LCO and LLZ proceed above 700 °C but are insignificant up to 1050 °C.[33] Tsai et al. prepared a rather thick cathode layer on an LLZ pellet by brush-painting and subsequent heating at 1050 °C for 30 min.[34] The cell exhibited a large area-specific capacity (ASC) of 1.6 mAh cm^{-2} (113 mAh g^{-1}) at a current density of 50 μA cm^{-2} at 50 °C. Ihrig et al. succeeded in decreasing the sintering temperature to 675–750 °C under high pressure of 440 MPa by field-assisted sintering technique (FAST), in other words, spark plasma sintering (SPS).[35] The obtained cell showed an ASC of ≈1.2 mAh cm^{-2}. Ohta et al. developed the cold-sintering process (CSP), in which a cathode layer consisting of NCM and LLZ was co-sintered on the solid electrolyte layer of LLZ.[36] In this process, Li^+ in LLZ particles was partially substituted with H^+ (LLZ-H) and were sintered in molten salt of LiOH and $LiNO_3$, which also played the role of Li supplier to compensate for extracted Li^+ in LLZ-H. After the CSP at 400 °C and 98 MPa, the cell of Li | LLZ | NMC showed a large initial discharge capacity of 1.7 mAh cm^{-2} (130 mAh g^{-1}) at a current density of 40 μA cm^{-2} at 25 °C. In these works, with the aid of high pressure at an elevated temperature in FAST/SPS and CSP, electrochemically active contacts were prepared at the interfaces between the active materials and the solid electrolytes. However, these processes are less compatible with the mass production of large-scale ceramic ASSBs. In addition, the pressure-assisted sintering processes cause residual stress in the materials.[37] The residual stress would affect electrochemical properties[37–39] and might promote fracture of microstructure in ceramic ASSBs that causes deterioration of battery performance.[34]

One of the strategies to reduce sintering temperature without applying pressure is liquid phase sintering (LPS). In LPS, low melting point additives form a liquid phase wetting the surface of particles of the main components and promoting the main components sintering by the rearrangement and the solution-reprecipitation mechanisms.[40] Several studies on LPS of LLZ systems have been reported by the group of Tadanaga and Rosero-Navarro.[41–43] They revealed that additives, such as Li_3BO_3 or LBSCA (Li_2O-B_2O_3-SiO_2-CaO-Al_2O_3), promote the densification of LLZ to improve conductivity, but the processes required a rather long time (10–36 h). Here, we developed a novel pressure-less sintering technique or quick liquid phase sintering (Q-LPS) to fabricate densely packed cathode composite layers. LiOH was used as a sintering additive to form the liquid phase. According to Rosero-Navarro et al., LiOH was less effective in improving the ionic conductivity (8×10^{-7} S cm^{-1}),[42] possibly because LiOH decomposes above its melting point (462 °C) and generates Li_2O and H_2O. LiOH was also used in the flux growth of LLZ at 700 °C[44] and LCO at 500 °C,[45] indicating that molten LiOH would play the role of the solvent for both LLZ and LCO. In Q-LPS, the temperature rapidly elevated to the process values forcing the LPS to proceed before the decomposition of all LiOH. The difficulty in developing ceramic ASSBs, especially garnet-based ceramic ASSBs/ASSLBs, comes from the fact that the battery performance depends on materials, processes, and architectures.[46,47]

2. Results and Discussion

2.1. Cells before the Optimization

Figure S1a, Supporting Information, shows an optical image of the half-cell of LLZT | LCO. A cathode composite layer of LLZT | LCO is printed and baked on an LLZT pellet. Charge–discharge curves of a cell prepared by Q-LPS before optimization are shown in Figure S1b, Supporting Information. The initial charge capacity was 50 mAh $(g\text{-LCO})^{-1}$ and the discharge capacity dropped to ≈10 mAh $(g\text{-LCO})^{-1}$. The cell performance was poor, but it should be noted that the cell showed a certain capacity at room temperature despite a rather high loading of LCO of ≈7 mg cm^{-2}. The cross-sectional image of the cathode

composite layer is shown in Figure S2, Supporting Information (videos of 3D internal structure reconstructed from focused ion-beam [FIB]-scanning electron microscope [SEM] images are also available in Supporting Information). The energy-dispersive X-ray spectrometer (EDS) mapping images in Figure S2b, Supporting Information, suggest that the bright and grey particles are LCO and LLZT, respectively, while the dark background is the void filled with the epoxy resin used to avoid the collapse of the cathode layer during the FIB process. Although the cathode layer is very porous (≈50%), there are interconnections among LLZT particles (indicated by orange circles), among LCO particles (red), and between LLZT and LCO particles (blue). On the other hand, scanning transmission electron microscope (STEM)-EDS images (Figure S3, Supporting Information) clearly show the formation of the interphase between LLZT and LCO particles and suggest the interphase mainly consists of La, Co, and O. Furthermore, selected-area electron diffraction (SAED) pattern was fitted with LCO and La_4LiCoO_8 from the crystal structure database. The ionic conductivity of La_4LiCoO_8, which was synthesized by a solid-state reaction, was estimated to be $\approx 10^{-10}$ S cm^{-1} at 25 °C (Figure S4, Supporting Information). The very low ionic conductivity of La_4LiCoO_8 indicates that the resistance of the 100-nm-thick interphase would be as large as 10^5 Ω cm^2. Starting with this cell, materials, processes, and architectures were optimized.

2.2. Material Optimization: Solid Electrolytes in Cathode Composite Layer

On the interphase of La_4LiCoO_8, we assumed the following reactions inside the cathode layer

$$Li_{6.5}La_3Zr_{1.5}Ta_{0.5}O_{12} \rightleftarrows Li_{6.5}La_{3-2x}Zr_{1.5}Ta_{0.5}O_{12-3x} + xLa_2O_3 \quad (1)$$

$$2La_2O_3 + LiCoO_2 \rightarrow La_4LiCoO_8 \quad (2)$$

As La_2O_3 was not detected in the original LLZT synthesized at 900 °C, it is supposed that Equation (1) was induced by Equation (2): in the original LLZT, Equation (1) was left-leaning, and La_2O_3 was too little to be detected by X-ray diffraction (XRD). However, when La_2O_3 was reduced by Equation (2), Equation (1) shifted to the right. In addition, Equation (2) was promoted by LiOH, which was confirmed experimentally. As shown in Figure S5, Supporting Information, La_4LiCoO_8 was formed at 900 °C even without LiOH, but LiOH promoted the reaction. Possibly the molten LiOH played the role of a solvent for La_2O_3 and $LiCoO_2$ to facilitate the reaction. To suppress the La-extraction from LLZT, $Li_{6.5}AE_{0.1}La_{2.9}Zr_{1.4}Ta_{0.6}O_{12}$ (AE = Ca, Sr, and Ba: LLZT-AE) was employed, in which AE at the La site and would reduce the chemical potential of La_2O_3 and/or hinder La migration in the LLZT.

Figure S6, Supporting Information, and **Figure 1**a show XRD profiles of the cathode layers consisting of LLZT-AE. While the cathode layer using pristine LLZT shows a weak shoulder around 33.6° that is attributed to La_4LiCoO_8 (tetragonal phase (PDF#01-083-1842) or orthorhombic phase (PDF#01-089-4701)),[48] neither shoulder nor peak was confirmed for the cathode layers using LLZT-AE. Note that a peak around 31.8° (the strongest peak of La_4LiCoO_8) can also be attributed to Li_2CO_3, a common impurity of LLZ. Thus, it is difficult to use this peak to detect La_4LiCoO_8. Figure 1b,c compares charge/discharge curves and electrochemical impedance spectra (EIS) of the cells with the cathode layers consisting of LCO and LLZT-AE. The cell with LCO + LLZT-Sr cathode exhibited the largest initial charge capacity (139.8 mAh g^{-1}) reaching the practical capacity of LCO (140 mAh g^{-1}). The capacity of LCO + LLZT-Ca was as low as LCO + LLZT. This can be explained based on the EIS results discussed below. In the Nyquist plots of EIS recorded at 3.95 V after three cycles, a semi-circle with a specific capacitance of $\approx 10^{-6}$ F cm^{-2} was observed for all cells. The intercept of the semi-circles on the real axis at a higher frequency limit corresponds to the resistance of the solid electrolyte layer (i.e., the resistance of the LLZT pellet with a thickness of ≈0.9 mm), and the semi-circle in the middle-frequency region is attributed to the charge transfer resistance from both cathode and anode interfaces. Here, the charge transfer resistance on the anode (Li | LLZT) is lower than 10 Ω cm^2,[49] and therefore, the main contribution comes from the cathode interface, that is, interfaces between LLZT-AE particles and LCO particles inside the cathode layers. The charge transfer resistance from the cathode side increased in the order of LLZT-Ca < LLZT-Sr ≈ LLZT < LLZT-Ba, which was not consistent with the order of the discharge capacity. This discrepancy could be explained by two resistances: 1) the solid electrolyte resistance in the cathode layer and 2) the charge transfer resistance on the interface of LLZT-AE | LCO. As shown in Figure 1d, the initial capacity seems to correlate with the ionic conductivity of LLZT-AE except for the pristine LLZT that formed impurities.[50] In the cathode layer with LLZT-Sr, the Li-ion conduction is faster than the others, and more LCO particles can contribute to the electrochemical reaction. In comparison with LLZT-Sr, Li-ion conduction in the cathode layers with LLZT-Ca is slower, and the cell voltage reaches the upper limit (4.2 V vs Li/Li$^+$) earlier, resulting in low capacity. On the other hand, the resistance obtained by EIS mainly focuses on the charge transfer resistance, which is related to the contact area and the interphases between LCO and LLZT-AE. The charge transfer resistance would also be influenced by the resistance between the cathode layers (LLZT-AE + LCO) and the solid electrolyte layer (LLZT). The cathode layers with different LLZT-AE were printed and sintered on the LLZT pellets in the same condition, and the particle size and shape of all LLZT-AE were similar. Thus, the difference of LLZT-AE in the cathode layer would cause little difference in the influence on the charge transfer resistance. Here, we concluded that LLZT-Ca surpasses Sr and Ba members in suppressing interphase formation. In this study, LLZT-Ca was used and denoted as LLZT.

2.3. Process Optimization: Pre-Hot Press and Heating

The high porosity of the cathode layers (Figure S2, Supporting Information) leads to poor electrochemical properties because of their mechanical fragility. The high porosity is partly caused by screen printing. On the other side, as the cathode composite particles were dispersed in α-terpineol, a large void remained after α-terpineol evaporation. To reduce the porosity,

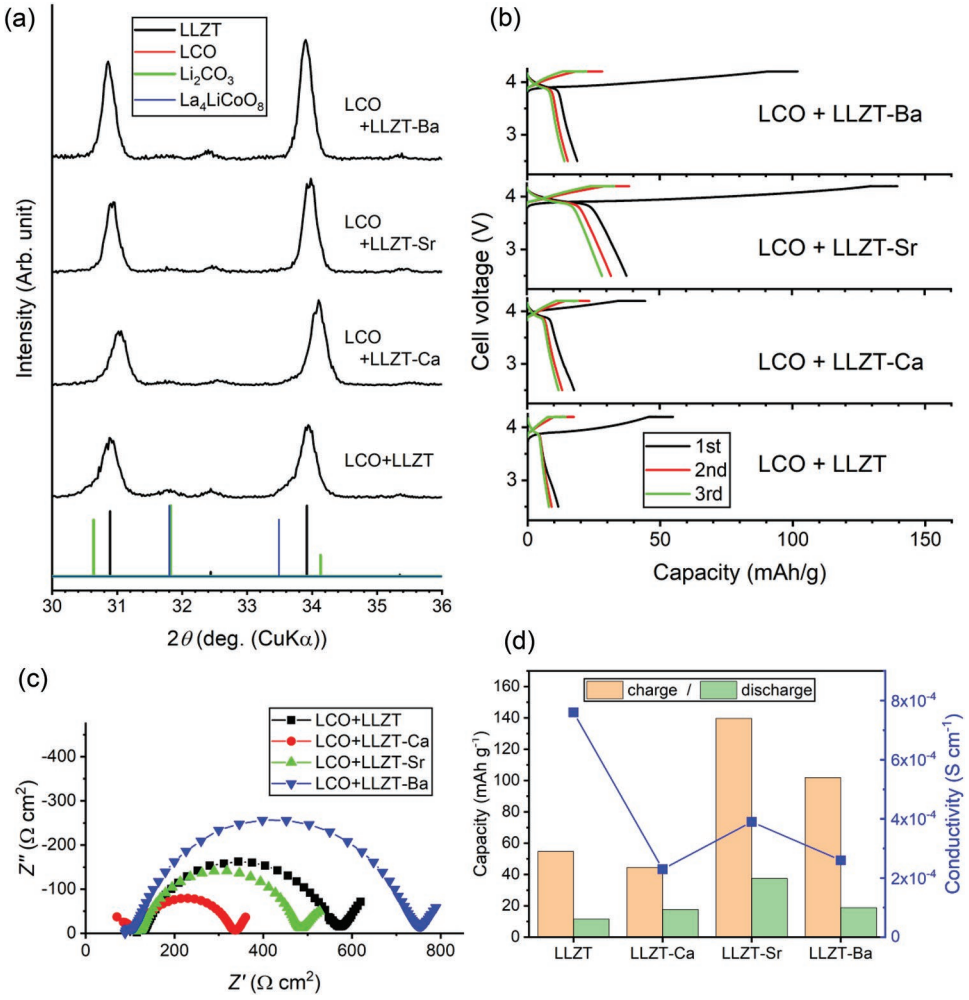

Figure 1. a) Magnified XRD profiles of the cathode layers consisting of LCO and LLZT-AE (AE = Ca, Sr, Ba). XRD profiles for the whole range are shown in Figure S6, Supporting Information. b) Charge/discharge curves of the cells using LLZT-AE (8 mg-LCO cm^{-2}, 0.01C, 25 °C). c) Nyquist plots of EIS for the cells at 3.95 V. d) Initial capacity of the cells using LLZT-AE and the ionic conductivity of LLZT-AE at 25 °C.

the influence of some pressing processes (cold isostatic press or hot press) before Q-LPS was studied. Hot pressing with a relatively mild pressure of ≈300 kPa at 350 °C resulted in better battery performance (Figure S7, Supporting Information).

In Q-LPS, the sintering proceeds in a temperature range where LiOH is not thermodynamically stable, and therefore Q-LPS is a non-equilibrium process. LiOH starts to decompose above the melting point (462 °C) and forms high melting-point Li_2O (1438 °C) that does not promote LPS. However, some LiOH remains in the molten state above 462 °C due to the finite decomposition rate, which promotes the sintering of the cathode layers by rearrangement and solution-reprecipitation processes until all LiOH decomposes. Therefore, the degree of sintering depends on the heating method. Figure S8, Supporting Information, compares the electrochemical performances of the cells prepared by the infrared gold image furnace and a muffle furnace. In both furnaces, the cells were heated at 900 °C for 10 min with a ramp rate of 50 K min^{-1}. A higher capacity was obtained for the cell heated in the infrared furnace, directly heating materials that absorb infrared radiation. Figure S9, Supporting Information, shows diffuse reflection UV–vis-near IR spectra of materials that may be included in the cells, and the calculated blackbody spectrum at 1500 K is also shown in the spectra, which corresponds to the emission spectrum of the infrared gold image furnace. The infrared radiation from the furnace directly heats the LCO particles in the cathode layers, while the solid electrolyte layer is less heated due to low IR absorbance by LLZT. As a result, the cathode layer is rapidly heated, and LiOH melts, sintering the LLZT and LCO particles. In the case of a conventional furnace, objects are heated by thermal convection and diffusion, which are rather slow processes. More LiOH would decompose, during the relatively slow increase in the local temperature, resulting in less LPS.

2.4. Architecture Optimization: Particle Shape

The porosity of the cathode layers could be further reduced by modifying the particle shape of LCO. **Figure 2** compares two LCO powders: spherical powder (LCO (s)) and plate-like powder (LCO (p)). As the particle size is close to that of the LLZT powder, better packing was expected. The porosity of

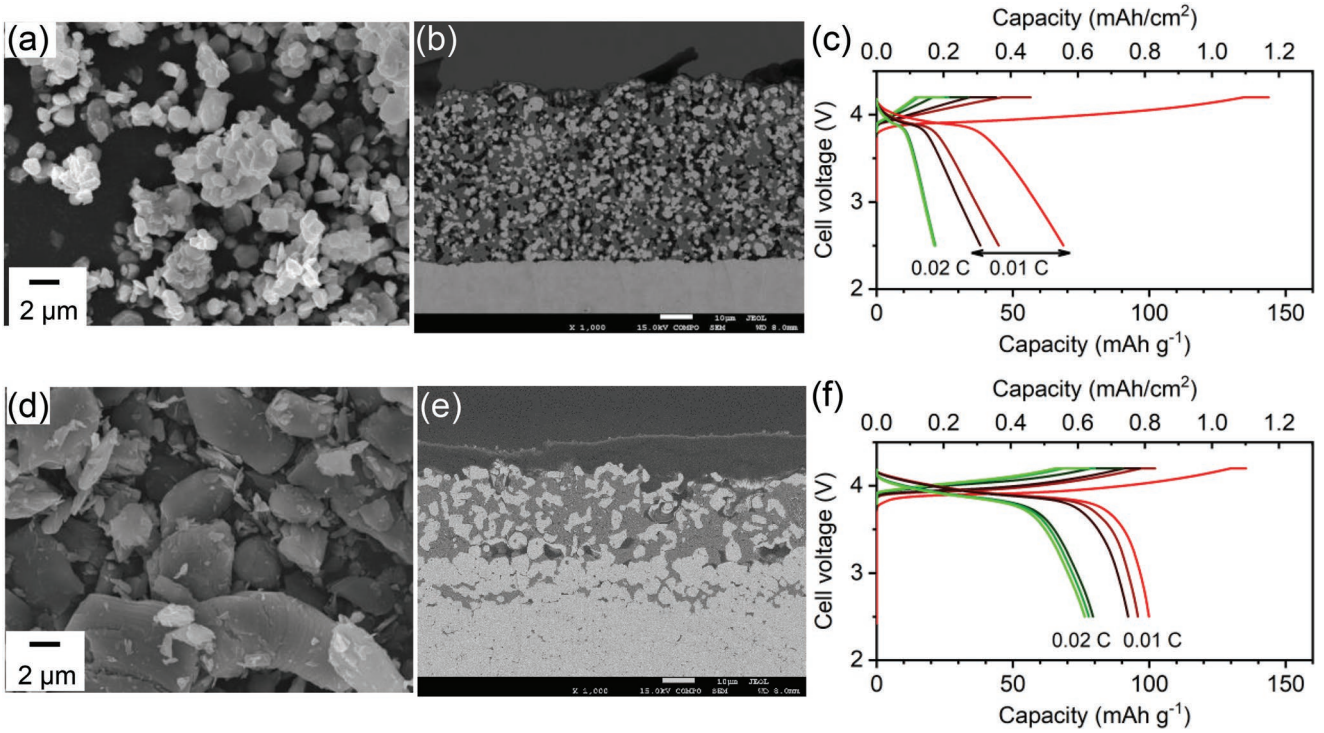

Figure 2. a,d) SEM images of LCO (s) and LCO (p) powders, respectively. b,e) Cross-sectional SEM images of the cathode layers prepared by the pre-hot press and subsequent Q-LPS using LCO (s) and LCO (p), respectively. c,f) Charge/discharge curves of the cells using LCO (s) and LCO (p), respectively. The cells consist of 8 mg-LCO cm^{-2} and are operated at 0.01 C and 25 °C.

the cathode layers prepared by Q-LPS without the pre-hot press estimated from the cross-sectional images using ImageJ software[51] was ≈50% regardless of the particle shape (Figure S2, Supporting Information). The pre-hot press before Q-LPS reduced the porosity to 23% and 3% for the cathode layers with LCO (s) and LCO (p), respectively (Figure 2b,e). Unexpectedly, a very dense cathode layer was obtained with LCO (p). The difference in the porosity influenced the capacity retention, as shown in Figure 2c,f. The cathode layer with LCO (p) showed better cycle ability, although the initial charge capacity reached the practical value for both LCOs.

As shown in Figure S10, Supporting Information, the screen-printed cathode layer using LCO (p) particles were aligned on the substrate (Figure S10b, Supporting Information) with *c*-axis orientation (Figure S10c, Supporting Information), while little preferential orientation was confirmed for LCO (s). One might think that the better capacity retention of the LCO (p) is due to the crystal orientation because of the anisotropic volume change of the LCO crystalline lattice during charge/discharge.[52] However, the preferential orientation of LCO (p) was reduced by increasing the process temperature of Q-LPS. The XRD suggested no specific orientation for the cathode layers with LCO (p) after Q-LPS at 900 °C as indicated in Figure S11a–d, Supporting Information. Therefore, the better cyclability of LCO (p) is due to the dense structure. When we carefully compare Figure S10a,b, the screen-printed cathode layer is thinner for LCO (p) than for LCO (s) for the same loading. Further, Figure 2b,e shows that the LLZT particles in the sintered cathode layer are larger for LCO (p) than for LCO (s). These results indicate that the planar shape of LCO (p) is easily densified by the printing and pre-hotpress to promote grain growth due to the solution-reprecipitation process proceeding during the very short heating time of Q-LPS.

2.5. Process Optimization: Sintering Temperature

The influence of the sintering temperature on the cell performance was also investigated. The strong *c*-axis orientation of the LCO crystalline in the cathode layer remained in the cathode layer sintered at 800 °C. The crystalline orientation disappeared with increasing the sintering temperature, suggesting the random orientation after the solution-reprecipitation processes during Q-LPS. The battery performance of the cells sintered at different temperatures is shown in Figure S12a–d, Supporting Information. The cells sintered at lower temperatures exhibited lower capacity, while those sintered at 900 and 950 °C showed higher capacity. This is because of the dense contacts at the interfaces of LLZT | LCO, LLZT | LLZT, and LCO | LCO, resulting from the solution-reprecipitation process (Figure 2d).

2.6. Cells after the Optimization

Figure 3 shows the SEM-EDS images of the cathode layer of the optimized garnet-based ASSLB after 50 charge/discharge cycles. Obviously, the LCO and LLZT grains were co-sintered to form a dense cathode layer. LCO and LLZT particles form a bi-continuous structure to create electron and ion networks

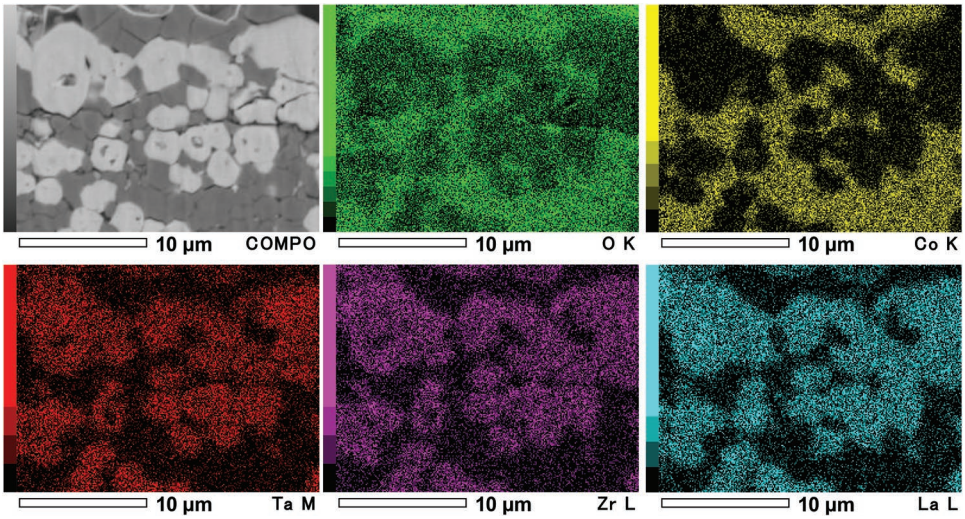

Figure 3. SEM-EDS images of the cathode layer consisting of LCO | LLZT-Ca prepared by Q-LPS after 50 charge/discharge cycles.

in the cathode layer. Some cracks could be confirmed, which will be discussed later. The interfaces of LCO and LLZT particles were further investigated by STEM-EDS shown in **Figure 4**. The cell was charged/discharged for six cycles. The

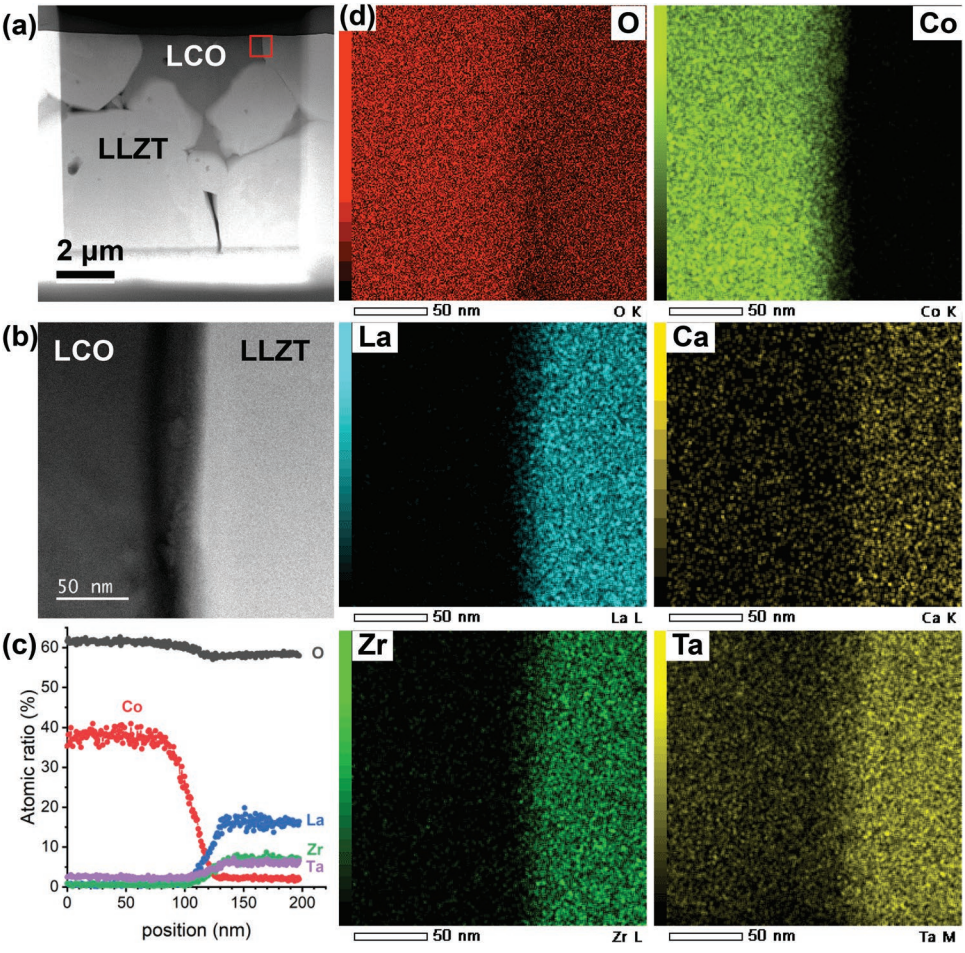

Figure 4. a) Dark field STEM image of the cathode layer consisting of LCO | LLZT-Ca prepared by Q-LPS. b) Magnified image for the red rectangle in panel (a). c) EDS line profiles along the horizontal direction in panel (b). The signal intensity was averaged for the vertical direction. d) EDS mapping images for the panel (b).

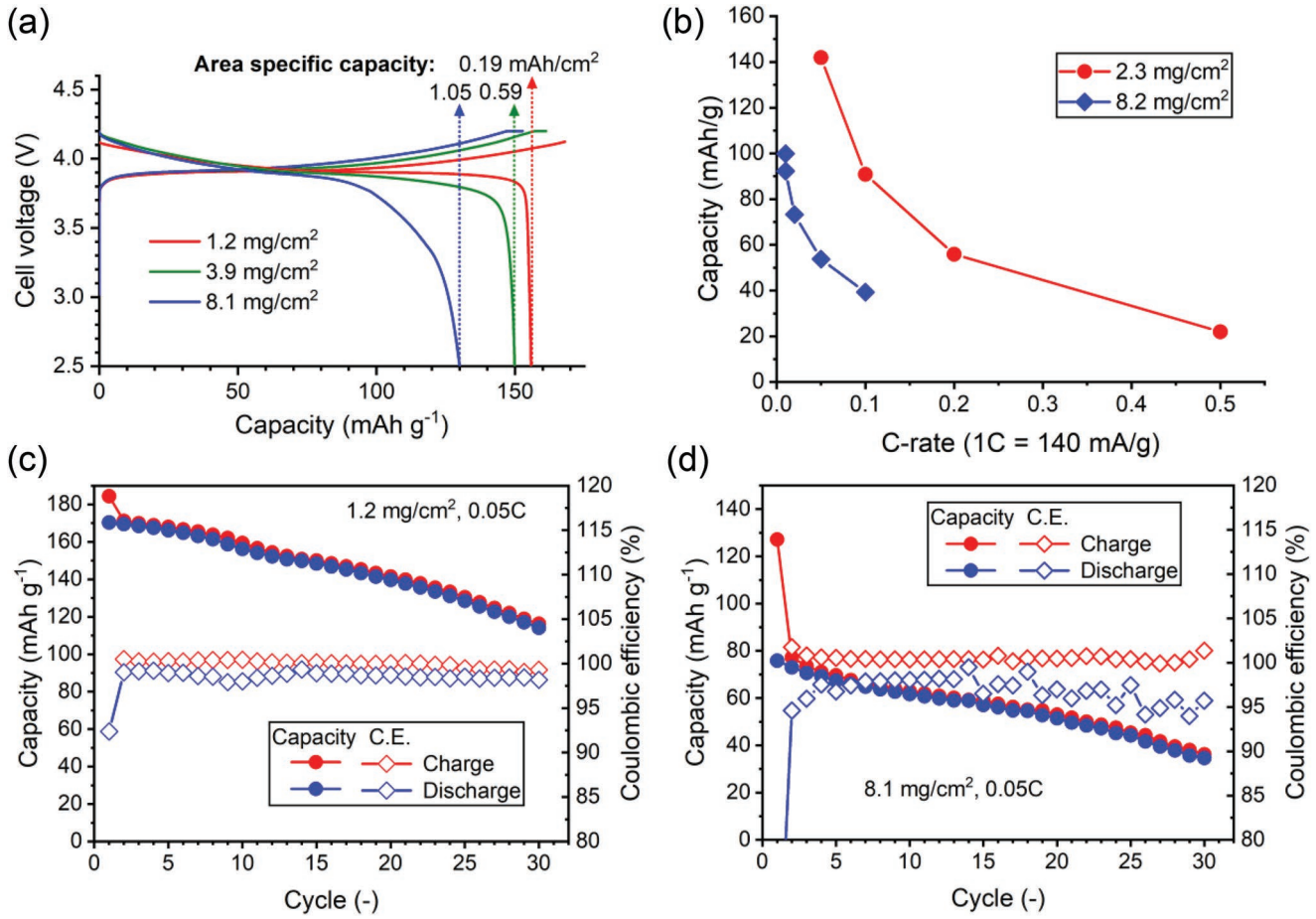

Figure 5. Battery performance of the cells prepared by Q-LPS. a) 1st charge/discharge curves for the different LCO-loading at 0.01 C, b) rate capability, c,d) cyclability for 1.2 and 8.1 mg cm^{-2}, respectively.

contact between LLZT and LCO is dense, and no interphase is confirmed. The composition gradient with a thickness of 20–25 nm is caused by overlapping LCO | LLZT grains at the interface tilting to the incident electron beam. A slightly high Ta level for the whole region is due to the Ta-M emission from the surrounding region excited by characteristic X-rays of the other elements. Therefore, element interdiffusion across the interface is negligible.

Figure 5 shows the battery performance of the cells prepared by Q-LPS. The cathode loading was controlled by simply changing the screen-print number. Although the cell with a cathode loading of 8.1 mg cm^{-2} showed a larger irreversible capacity than the others, the first discharge capacity was as high as 130 mAh g^{-1} corresponding to the ASC of 1.05 mAh cm^{-2} (Figure 5a and Table S1, Supporting Information). The relatively large ASC and the simple printing/sintering processes are beneficial for large-scale ceramic ASSBs/ASSLBs. Interestingly, the capacity for the lower loading is higher than the practical capacity of LCO (140 mAh g^{-1}). The high capacity was reversible and maintained for over 15 cycles (Figure 5c). The reason for the higher capacity is not clearly understood. Some of the possible mechanisms are the partial redox reaction of the solid electrolyte, the electrode-potential reduction caused by the mechanical stress,[53] and/or the interphases (La_4LiCoO_8 or low-temperature phase of $LiCoO_2$ (LT-LCO)).[54] As Fakkao et al. revealed, the compressive stress on LCO decreases the electrode potential at the same state of charge.[53] When the electrode potential is decreased by 100–200 mV, LCO may be overcharged at an electrode potential of 4.2 V versus Li/Li^+. However, the influence of the stress is too small (≈0.05–0.1 mV for −20 MPa) to cause the over-charging of LCO,[53] even though large internal stress of ≈1 GPa is applied during charge/discharge (discussed in Sections 2.1–2.7). The LT-LCO (spinel phase) exhibits a plateau at ≈80 mV-lower electrode potential than a high-temperature phase of LCO (layered rock salt phase).[54] However, the LT-LCO exhibits a low discharge plateau at 3.4 V versus Li/Li^+, which was not observed in the present study. The origin of the high reversible capacity is still unclear, which should be clarified in future studies.

Figure 5b–d shows the rate capability and the cyclability of the cells with high and low LCO loading. The cell with the high cathode loading showed a discharge capacity of 57% at 0.05 C and 40% at 0.10 C in comparison with 0.01 C (Figure 5b). The low LCO loading showed better rate capability than the high LCO loading. It should be noted that the reduced capacity includes the influence of deterioration during the charge/discharge cycles. For the high LCO loading (Figure 5d), capacity retention was 46% after 30 cycles at 0.05 C, whereas for the low

LCO loading was 67%. Coulombic efficiency was higher than 95% after three cycles. Note that the Coulombic efficiency for the charge is almost 100%, while that for the discharge is lower. This means that the deterioration of the cell occurs at the end of the charge or during the discharge. Furthermore, the loading-dependent capacity retention suggests that the deterioration is mainly caused by mechanical issues. The cell deterioration will be discussed in detail later.

Table S1, Supporting Information, compares the battery performances of the garnet-based ASSBs/ASSLBs in this work and those reported in the literature.[30,32,34–36,55,56] The variety of the test conditions might cause confusion; however, here we compare the performance from the viewpoint of the large-scale batteries. An areal capacity of 3 mAh cm^{-2} or higher values would be required for practical application.[55] Unfortunately, any cells have not satisfied the demand, but among cells that exhibit a higher capacity than 1 mAh cm^{-2}, the cell prepared by the combination of Q-LPS with pre-hot press shows some advantages with respect to the low process pressure (300–500 kPa) and the low discharge temperature (25 °C).

Further study was conducted using the cells with higher LCO loading to clarify the issues to be solved toward large-scale garnet-based ASSLBs. The temperature-dependent battery performance was investigated to understand the rate-determining step (RDS) of the cells. The charge/discharge cycles were repeated 20 cycles in advance to minimize the influence of the cycle-induced capacity fading. The discharge capacity (0.05 C) was recorded at the temperature range from 50 to 10 °C after 3-h stabilization at each discharge temperature, while the cell was always charged at 50 °C with CC-CV mode (0.05 C). The capacity decreased with temperature reduction, and the apparent activation energy ($E_{app.}$) was 0.31 eV (**Figure 6**a,b). The temperature-dependent EIS was also recorded (Figure 6c), in which the cell voltage was held at 3.9 V. The cell voltage was chosen to avoid the deterioration at higher cell voltage during the measurement as indicated by the asymmetric Coulombic efficiency for charge/discharge processes (Figure 5c,d). The Nyquist plots of the EIS consisted of three parts, which are attributed as in Section 2.2: i) the resistance of the solid electrolyte layer (R_{SE}) for a high-frequency region (>600 kHz), ii) the charge transfer resistance (R_{ct}) for a middle-frequency region (600 k–10 Hz), and iii) the Li-ion diffusion in the LCO particles (Z_W) for a low-frequency region (<10 Hz). As shown in Figure 6d, the activation energy of R_{SE} and R_{ct} were 0.30 and 0.60 eV, respectively. Compared with these activation energies, the apparent activation energy of the capacity agrees well with that of R_{SE}. However, the contribution of R_{SE} is not significant in the total impedance ($R_{SE} + R_{ct} + Z_W$), especially at lower temperatures (see Figure 6d). Therefore, R_{SE} would not be the RDS of the garnet-based ASSLB. Another candidate for the RDS would be Z_W. The activation energy of the Li-ion diffusion in LCO is 0.26–0.32 eV,[57–59] which is in good agreement with $E_{app.}$ of 0.31 eV. These results suggest that the diffusion length in the LCO particles must be shortened to improve the power density, as well as the low-temperature performance of the cells. The long diffusion path in LCO would be caused by several issues: i) the grain size of the LCO, ii) the ion migration network in the cathode, and iii) the contact between LLZT and LCO. For the LCO with grain size after Q-LPS of ≈10 µm (Figure 2d), the finite diffusion length is 5 µm if all surface is covered by an electrolyte. The diffusion length l in a 2D lattice can be roughly estimated by the following equation

$$l \approx \sqrt{4\tilde{D}t} \tag{3}$$

where $\tilde{D}$ and t are the chemical diffusion coefficient of lithium-ion and diffusion time, respectively. Assuming $\tilde{D}$ of 10^{-11} cm^2 s^{-1} and t of 20 h (corresponding 0.05 C, 7 mA g^{-1}),[60] diffusion length would be 17 µm, which is long enough to charge/discharge all capacity. However, the results suggest that the capacity is limited by the Li-ion diffusion in the LCO, which means that the broken ion-migration network in the cathode and/or the poor contact of LLZT | LCO, which makes the effective diffusion path longer.

2.7. Deterioration of the Cell

Poor cyclability is one of the critical issues of the cells using oxide-based solid electrolytes. Although the cyclability could be improved by reducing the LCO loading (Figure 5),[30,32,55] the deterioration of the cell with high LCO loading was studied toward the practical large-scale garnet-based ASSLBs. EIS was recorded during charge/discharge cycles to study the deterioration of the cathode layer. The Nyquist plot showed R_{ct} was ≈100 Ω cm^2 and as low as R_{SE} in the beginning (3.9 V in the first charge). However, R_{ct} at 4.1 V was approximately six times larger than that at 3.9 V (**Figure 7**b). After the dramatic increase in R_{ct} in the first charging step, R_{ct} did not drop to the original value and monotonically increased for each voltage with cycles, as shown in Figure 7c,d.

As for the LLZT | LCO systems, two mechanisms of capacity fading have been reported: fractures and interphases.[47] Ihrig et al. reported that amorphous interphases are formed on the interfaces between LCO and LLZT after charge/discharge cycles,[61] which could be recovered by thermal treatment.[62] It is known that element interdiffusion is induced by electrochemical processes for sulfide-based ASSBs.[63] However, in our studies, such interphases could not be confirmed even after six cycles (Figure 4). Although the possibility of the interphases may not be completely denied, the major deterioration mechanism is supposed to be the fractures because of the loading dependence as shown in Figure 5c,d. This is also indicated by the dramatic increase and the subsequent monotonic increase in R_{ct} (Figure 7). If the interphase formation is the only mechanism, R_{ct} would saturate when the interphases are formed on all interfaces. The loading-dependent capacity retention also supports mechanical deterioration.

As pointed out by Tsai et al., the fracture in the cathode layer would be the most critical reason for the capacity fading,[64] which is induced by the internal mechanical stress of the cathode layer. Several stress types and fracture mechanisms are summarized in **Figure 8**a. The dynamic stress caused by the volume change of the active materials during charge/discharge would be a predominant stress leading to the fracture.[52] In addition, most of the ceramic ASSBs contain static stress introduced during their preparation: thermal and residual stress. The thermal stress depends on the process temperatures and

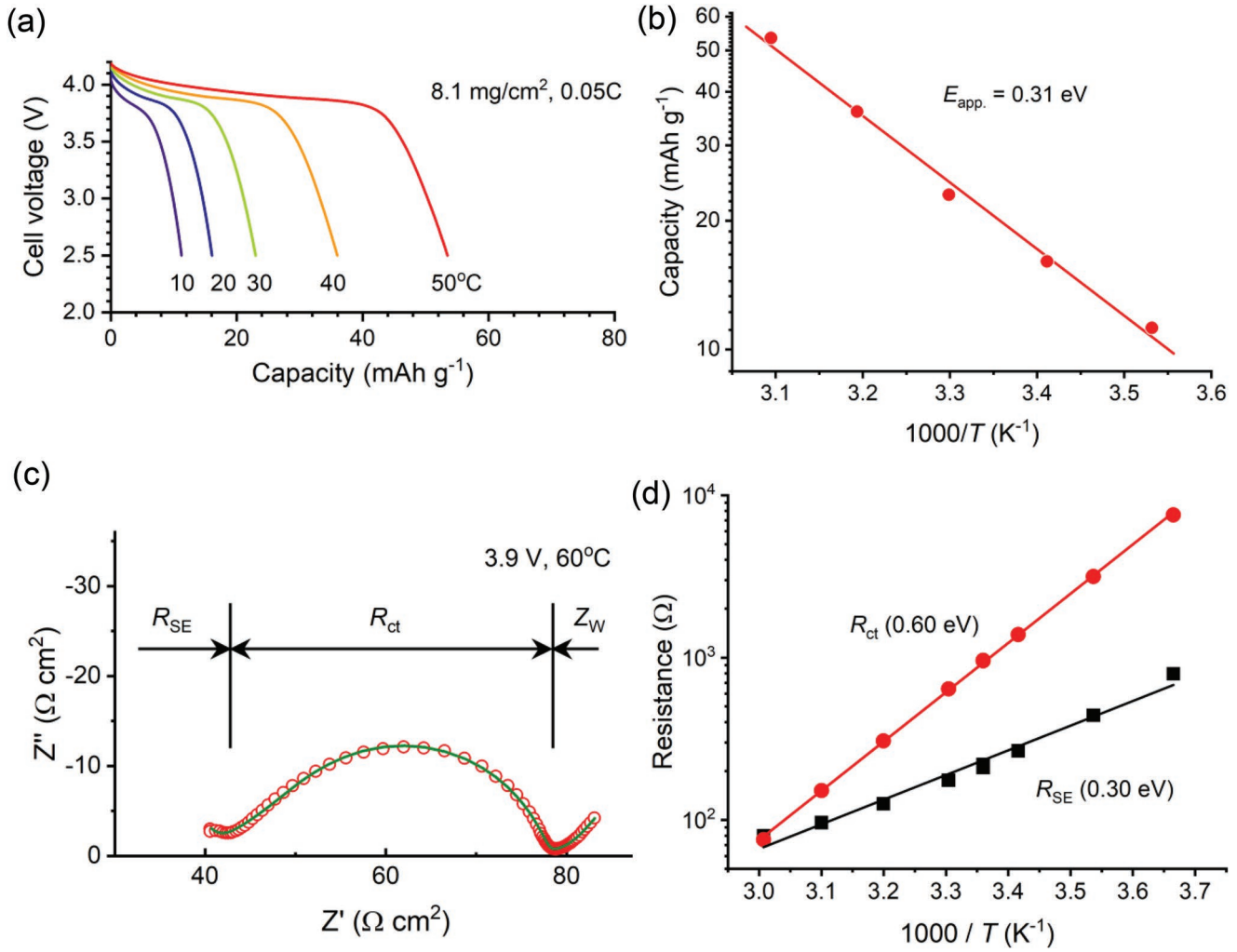

Figure 6. Temperature-dependent battery performance of the cell (8.1 mg-LCO cm^{-2}) prepared by Q-LPS. a) Discharge curves (the cell was always charged at 0.05 C, 50 °C), b) Arrhenius plot of the discharge capacity, c) Nyquist plot of the cell at 3.9 V, 60 °C), and d) Arrhenius plot of the resistance.

the difference in the coefficient of thermal expansion (CTE) of materials. CTE of LLZ and LCO are 1.5×10^{-5} and 1.3×10^{-5} K^{-1}, respectively, and would not cause significant thermal stress.[65] The residual stress would be significant for the high-pressure sintering processes.[37] Concerning the range/scale of the stress, the nano-stress is induced at the interfaces of LCO | LLZT, and the stress between the cathode and solid electrolyte layers would range from μm- to cm-scale.

Multiphysics simulation was conducted using a structure model shown in Figure S13a, Supporting Information, with parameters listed in Table S2, Supporting Information, to estimate the stress inside the cathode layer of the garnet-based ASSLBs during charge/discharge cycles. **Figure 9** shows the simulated stress distribution in the cathode layer at a charge capacity of 110 mAh g^{-1}, and stress values at several points in the cathode layer are shown in Figure S13c,d, Supporting Information. As von Mises stress distribution shows, extreme stress is applied inside the cathode layer during charge/discharge. Among various types of stress shown in Figure 9, maximum principal stress and shear stress are significant for the fracture of ceramics. Positive maximum principal stress is tensile stress, and the failure mechanism related to tensile stress is called mode I, while modes II and III are the crack growth induced by shear stress depending on the direction of the shear stress. As shown in Figure 9b and Figure S13d, Supporting Information, strong tensile stress (≈0.8 GPa) is applied to the LLZT in the cathode layer, which would induce fracture of LLZT by mode I. The shear stress on the LCO particle surfaces reaches 0.4–1 GPa (Figure 9d and Figure S13f, Supporting Information), which would cause separation of the LCO | LLZT interfaces. Such high internal stresses are due to the high Young's moduli of LCO (191 GPa) and LLZT (150 GPa): subtle strain causes large stresses. Note that the volume change of LCO is anisotropic, while the isotropic volume change model was employed in this simulation to simplify the calculation. Therefore, the stress distribution is more complicated in the actual cathode layer, and the shear stress would also be applied to the grain boundaries of LCO particles, which might break electron networks.

For the cells prepared by Q-LPS, at least four failure mechanisms were confirmed by SEM (Figures 3 and 8b–d): 1) broken electron networks (in the LCO grains and at the grain boundaries of LCO | LCO), 2) broken ion networks (in the LLZT grains

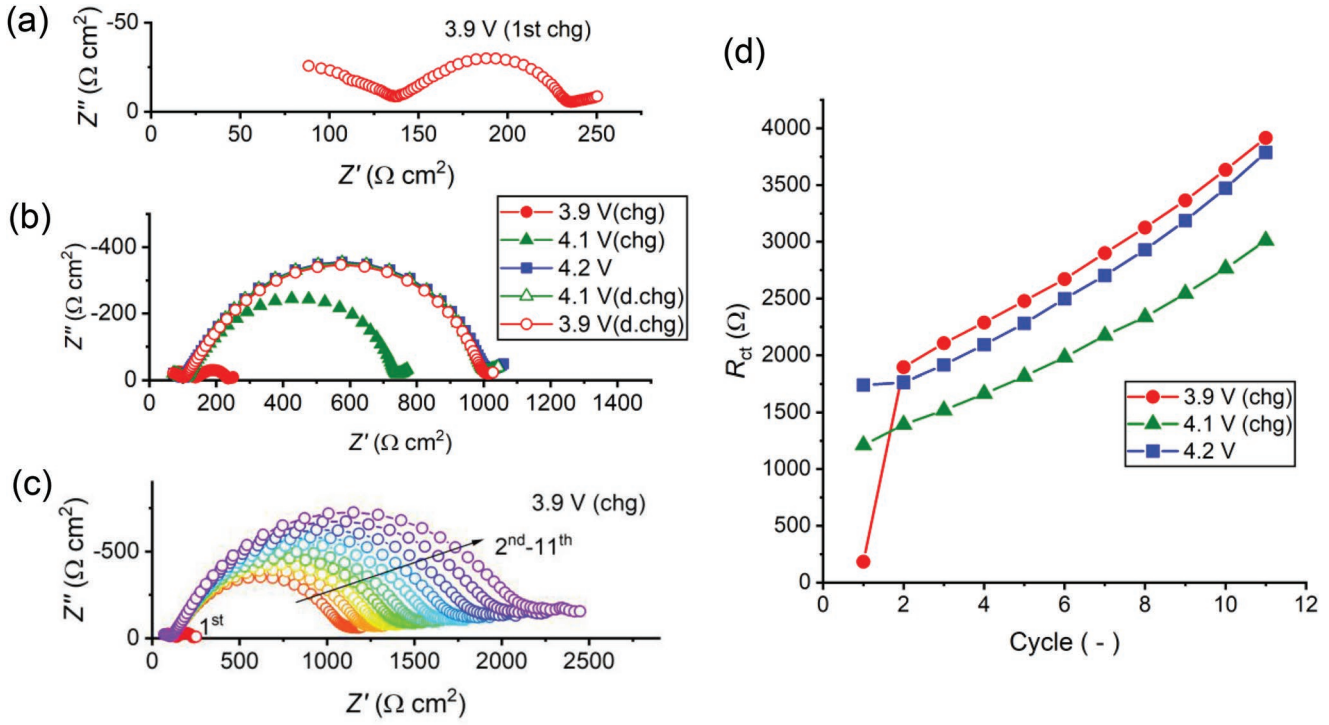

Figure 7. Cycle-dependent EIS. Nyquist plot of the cell a) at 3.9 V on the 1st charge, b) during the 1st charge/discharge, and c) at 3.9 V on the different cycles. d) Charge transfer resistance as a function of the cell voltage and the cycle.

and at the grain boundaries of LLZT | LLZT), 3) separation of interfaces of LCO | LLZT, and 4) delamination of the cathode layers. The delamination was significant for the cathode layer consisting of LCO (s) (Figure 8d). It should be noted that one crack would influence all active materials beyond the crack in the electron and ion networks. Therefore, the deterioration of the cells is more significant for the thicker cathode layers, which was experimentally confirmed (Figure 5).

As shown in Figures 3, 4, and 8, electron microscopes are useful tools to detect internal local structures and analyze the buried interfaces. However, these techniques are destructive and require mechanical processing: cutting, polishing, and/or thinning. These processes may also cause additional fractures in the cells, which would be hardly distinguished from the original fractures that induced capacity fading. X-ray computed tomography (X-ray CT) may be one of the non-destructive and in-operando techniques allowing analyzing inside of the solid.[66,67] However, its minimum spatial resolution is ≈100 nm, and the microcracks narrower than this limit cannot be detected. Furthermore, the specimens must generally be small (typically 1 mm in diameter or less) to allow enough X-ray transmission and mechanical processing would be required. The X-ray transmittance of LLZT is very low due to the heavy elements (La, Ta), which hinders the application of X-ray CT to garnet-based ASSLBs.

In this work, we indirectly speculated the fracture mechanisms (1)–(4) using the electrochemical results. The RDS study suggests that the partially broken interfaces between LCO |

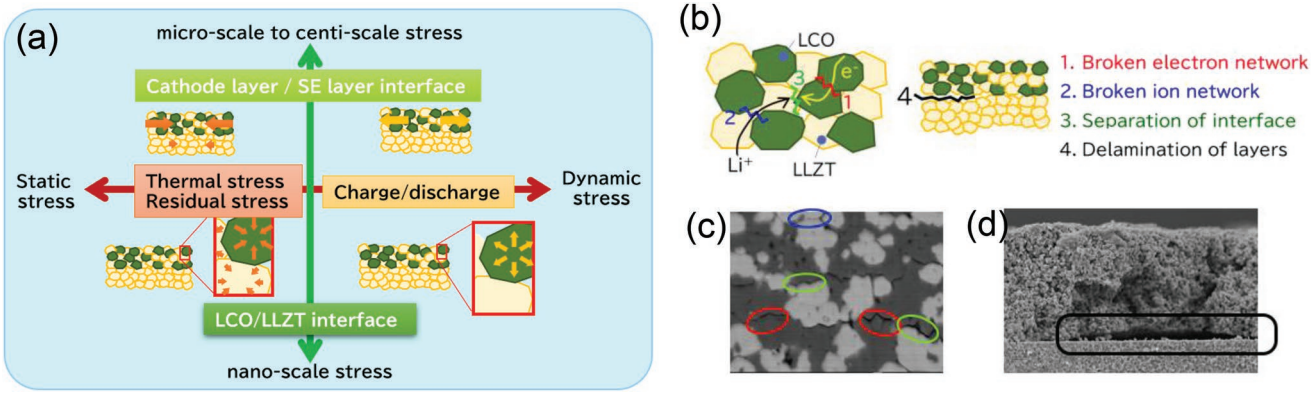

Figure 8. a) Classification of internal stress in the cells. b) Fractures and influences on the deterioration of the cells. c,d) Fractures observed in the cells after the charge/discharge tests.

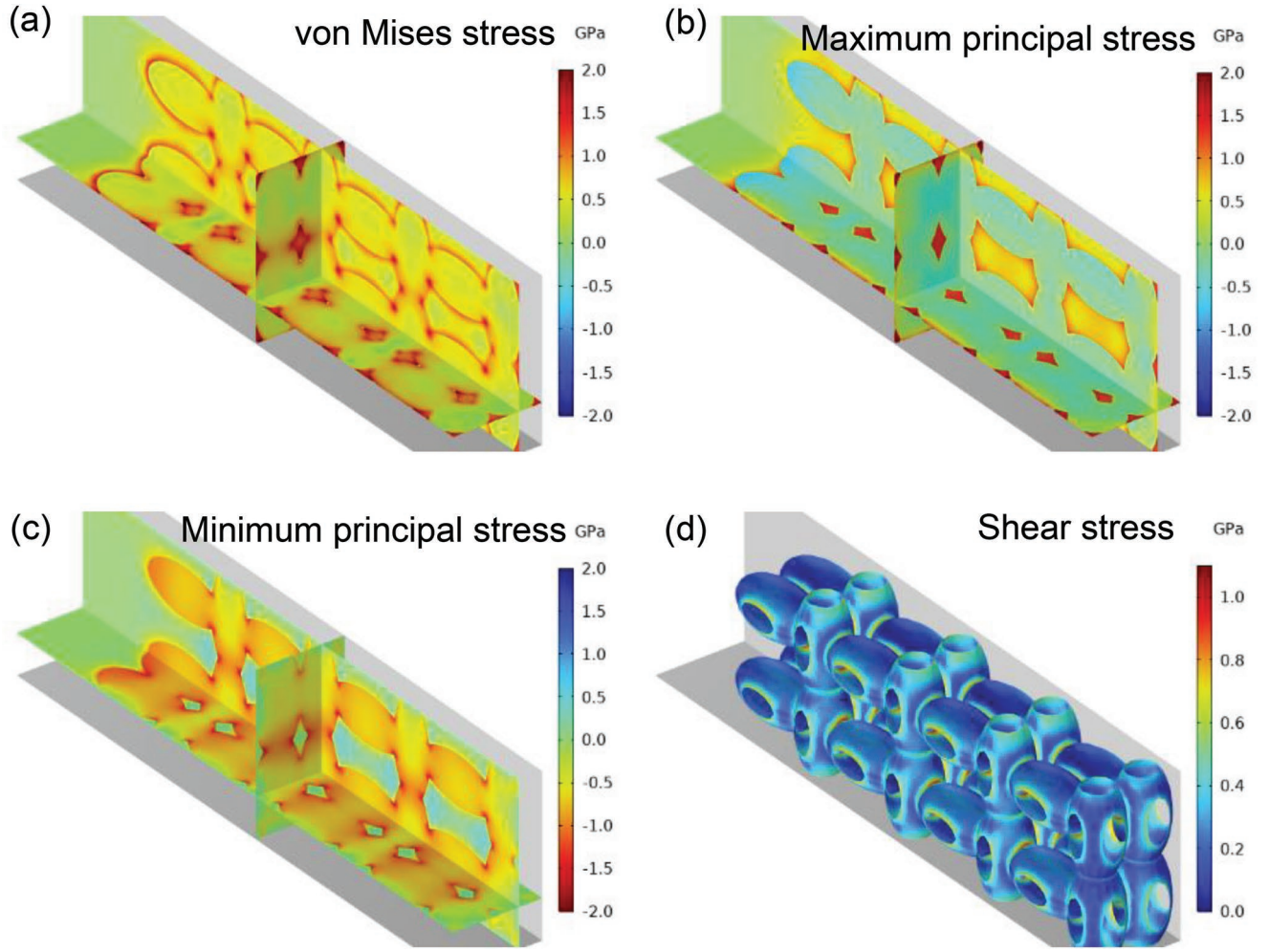

Figure 9. a–d) Simulated stress distribution in the cell of Li | LLZT | LCO at a charge capacity of 110 mAh g^{-1}. a) von Mises stress, b) maximum principal stress, c) minimum principal stress, and d) shear stress.

LLZT (failure mechanism (3)) result in a longer diffusion path in the LCO grains. Furthermore, another experiment was conducted to estimate the influence of the fractures related to ion conduction (failure mechanisms (2)–(4)): a drop of ionic liquid electrolyte (IL) was poured into the cathode layer after three charge/discharge cycles (Figure S14, Supporting Information). The IL addition increased the capacity (Figure S14b, Supporting Information) and reduced R_{ct} (Figure S14c, Supporting Information), but the capacity recovery was not enough in comparison to the initial charge capacity. When we carefully compare the discharge-curve profiles before and after the IL addition, the capacity in the high-voltage plateau region (>3.8 V) increased while that in the low-voltage region (<3.8 V) decreased. The capacity in the low-voltage region results from the distributed ionic/electronic resistance in the cathode composite. Therefore, the decreased low-voltage capacity by the IL addition means the repaired ionic network in the cathode layer increased the amount of "active" LCO particles. This result indicates the failure mechanisms (2)–(4). Furthermore, even after the IL addition, the capacity decreased with the cycle, suggesting the deterioration of the electron network (failure mechanism (1)).

From the above results, stress management is critical to realize the practical garnet-based ASSLBs. A few strategies may be possible to improve the durability of the cathode layers. One approach is to prepare a robust cathode layer and form stronger bonds at the interfaces, which may require high-pressure or high-temperature processes. Decreasing the sintering temperature of LLZ and/or active materials by element substitution might also be effective. Hayashi et al. successfully decreased the sintering temperature of LLZ to 750 °C by doping Ca and Bi and the addition of Li_3BO_3.[56] The ASSLB using this solid electrolyte exhibited good capacity retention of 92.8% at the 40th cycle. Another idea is a flexible cathode layer by introducing "soft" buffer materials that would absorb the active materials' volume change. Ihrig et al. introduced polymer electrolytes to the porous cathode composites of LCO and LLZ.[68] In this strategy, it would be important to optimize materials (Young's modulus, chemical/electrochemical stability), processes, and architecture (distribution, volume ratio of the soft material, and residual pores). The other strategy is to employ little-strain active materials. Like the well-known "zero-strain" anode material $Li_4Ti_5O_{12}$,[69] some cathode materials with little volume change have been reported.[54,70,71] These approaches would be

worth studying, and the introduction of new processes or materials would require re-optimization of the materials/processes/architectures.

3. Conclusions

In this study, a novel sintering technique of Q-LPS was developed to prepare the cathode layer of the garnet-based ASSLBs. Q-LPS was applied to the screen-printed cathode composite layers to promote sintering without high pressure, which would be suitable for the large-scaled ceramic ASSBs/ASSLBs. Materials and architectures were also optimized simultaneously to achieve the cells that exhibit a charge/discharge capacity of 1 mAh cm^{-2} and 130 mAh g^{-1} at room temperature. For further higher battery performance, the RDS and the deterioration of the prepared cells were investigated. It was revealed that the lithium-ion diffusion in the LCO particles is the RDS, which would be due to the incomplete interfaces of LCO | LLZT. Furthermore, other failure mechanisms of the broken electron network, the broken ion network, and the delamination of the cathode layers were experimentally confirmed. Three approaches would be proposed to overcome these issues: 1) to prepare the mechanically tough cathode layer, 2) to introduce soft materials to buffer the strain, and 3) to employ little-strain cathode materials.

4. Experimental Section

Solid Electrolyte Layer: A garnet-type solid electrolyte $Li_{6.5}La_3Zr_{1.5}Ta_{0.5}O_{12}$ (LLZT) was used as the solid electrolyte layer of the cells. The LLZT powder was synthesized by the solid-state reaction, which was pelletized by SPS. Although SPS was employed to obtain the pellets in this work, the sintering technique was irrelevant if the pellets were dense enough to reduce the solid electrolyte resistance and avoid the lithium penetration from the anode.[20,49] The synthesis and sintering processes of LLZT are described in detail elsewhere[20,37] and are briefly explained here. First, $LiOH{\cdot}H_2O$ (Kishida Chemical Co. Ltd., 99.0%), La_2O_3 (Kishida Chemical Co. Ltd., 99.99%), ZrO_2 (Kishida Chemical Co. Ltd., 99.9%), and Ta_2O_5 (Fujifilm Wako Pure Chemical Corp., 99.9%) were dry-mixed with a stoichiometric ratio by planetary ball-milling. 10%-excess Li was added to compensate for the Li loss during the subsequent high-temperature process. $LiOH{\cdot}H_2O$ was dried at 200 °C overnight and La_2O_3 was heated to remove water and CO_2 at 800 °C for 6 h before use. Then, the mixture of the starting materials was calcined at 900 °C for 12 h to obtain LLZT powder. Next, 0.5 g of the LLZT powder was poured into a graphite die and punched for SPS. The SPS was conducted under vacuum (≈10 Pa) at 900 °C with a ramp rate and a dwell time of 50 K min^{-1} and 10 min, respectively. After removing the graphite from the surface of the pellets by polishing them with emery papers, the LLZT pellets with a diameter and a thickness of 10 and ≈0.9 mm were obtained. The LLZT pellets exhibited a high relative density of 96–98% and a rather high total ionic conductivity of 8×10^{-4} S cm^{-1} with negligible grain boundary resistance.

Cathode Layer: The as-prepared LLZT powder or alkaline earth-doped LLZT (LLZT-AE; AE = Ca, Sr, and Ba) powders were used in the cathode composite. In LLZT-AE, AE substituted a La site with a composition of $Li_{6.5}AE_{0.1}La_{2.9}Zr_{1.4}Ta_{0.6}O_{12}$. The synthesis, structure, and ionic conductivity of the LLZT-AE are described elsewhere.[50,72] LiOH was deposited on the surface of LLZT or LLZT-AE particles by mixing additional LiOH (2 wt%) and LLZT and subsequent heating at 500 °C.[73]

Two types of LCO powders were used: spherical powder LCO (s) and plate-like powder LCO (p). LCO (s) with a diameter of ≈1 µm was synthesized as follows: first, $CoSO_4$ aqueous solution was mixed with oxalic acid to obtain precipitation of CoC_2O_4, which was calcined at 500 °C to produce Co_3O_4. After pulverization by ball-milling, Co_3O_4 powder was mixed with a stoichiometric amount of Li_2CO_3 and was calcined at 750 °C to obtain LCO (s). LCO (p) was prepared by ball-milling commercial LCO powder (Sigma-Aldrich, with an initial diameter of 10–20 µm). LCO powder was mixed with the LLZT or LLZT-AE powders (50:50 by volume) in acetone by using an agate mortar and a pestle and then dispersed in a solution of ethyl-cellulose in α-terpineol by a planetary centrifugal mixer (SK-300SII, Shashin Kagaku Co., Ltd.). The obtained viscous ink was printed to form a cathode layer with a diameter of 8 mm on an LLZT pellet by screen printing (MEC2400·T15A, Mitani Micronics Kyushu Co., Ltd.). The printed ink was dried at 80 °C on a hot plate. The printing/drying processes were repeated for 2–10 cycles, resulting in the loading of 1–8 mg-LCO cm^{-2}. The cathode layer on the LLZT pellet was degreased at 300–500 °C and was calcined in air at 900 °C for 10 min with a high ramp rate of 50–100 K min^{-1} using an infrared gold image furnace (RHL-P410C, Ulvac Riko, Inc.). A muffle furnace (FT-01X, FULL-TECH) was also used to study the influence of the heating method.

Cell Assembly: After preparing the cathode layer, the LLZT pellets were annealed at 700 °C in O_2 flow in a quartz tubular vessel to remove the Li_2CO_3 layer on the LLZT pellets.[14,44] Next, the tubular vessel was evacuated and transferred into an Ar-filled glovebox. Then, the opposite side of the cathode layer on the LLZT pellets was polished with emery paper (#400) and the Li anode was deposited at 250 °C on that surface by directly spreading molten Li. As the Li_2CO_3 layer was removed from the surface of LLZT, the surface of the LLZT pellets was sufficiently wetted by molten Li. After cooling, the cell of Li | LLZT | LCO was placed in a custom-made gas-tight vessel for electrochemical analyses. In the vessel, the cell was uniaxially pressed (300 kPa) by a coil spring.

Electrochemical Tests: Electrochemical tests of the cells were carried out on an HJ1020mSD8 (Hokuto Denko Corp.). In a typical test, the cells were charged with the constant current-constant voltage (CC-CV) mode up to 4.2 V and discharged with the CC mode down to 2.5 V. The charging/discharging rate was 0.01–0.1 C (1 C = 140 mA g^{-1}). Electrochemical analyses were conducted at 25 °C in a peltier cooled incubator (Mitsubishi Electric Engineering, CN-40A), and the temperature dependence was studied in an environmental test chamber (Espec Corp., SU-242). EIS was recorded at 3.9 V in a frequency range from 1 MHz to 0.1 Hz on an SP-300 (Biologic) or an HZ-Pro S4 (Hokuto Denko Corp.).

Structural Characterization: The different phases in the cathode layers were studied by XRD using a parallel beam X-ray source (CuKα (λ = 1.5418 Å), 45 kV, and 200 mA) on a SmartLab (Rigaku Corp.). The microstructure of the cells was investigated using a field-emission scanning electron microscope equipped with an energy-dispersive X-ray spectrometer (FE-SEM-EDS; JSM-7500FAM, JEOL Ltd.). For the cross-section analyses by the FE-SEM-EDS, the cross-section of the cells was polished by an Ar^+ ion beam (acceleration voltage: 6 kV) with an IB-09010CP cross-section polisher (JEOL Ltd.). 3D images of the cathode layer were also taken to analyze the interconnection among the particles using a FIB-SEM (SMF2000, Hitachi High-Tech Science Corp.). Detailed analyses of the interfaces between LCO and LLZT particles were investigated by an aberration-corrected STEM (JEM-ARM200F, JEOL Ltd.) equipped with a cold field-emission gun and two EDS analyzers. SAED patterns were recorded on the same microscope and analyzed in Crystal Maker software.

Multiphysics Analysis: Multiphysics analysis based on the finite element method was conducted using COMSOL 6.1 software with a battery design module. The model cell (Figure S13a, Supporting Information) consisted of a cathode layer, a solid electrolyte layer, and a lithium foil as an anode. The thickness of the cathode layer and the solid electrolyte layer was 15 and 10 µm, respectively. In the cathode layer, interconnected ellipsoidal LCO particles with three semi-axes lengths of 1.5, 0.75, and 0.75 µm were embedded in the LLZT matrix. The volume fraction of LCO was 53.5%. The parameters and conditions for the simulation are listed in Table S2, Supporting Information. First,

the charge curve and the time-dependent local Li concentration for the model cell were calculated using the LIB interface and the transport of diluted species interface. Then the volume change was analyzed using the solid mechanics interface. The local strain/stress was obtained using the local Li concentration. Here, the isotropic volume change model was employed to simplify the model, although actual LCO grains exhibit an-isotropic volume change.[52]

Supporting Information

Supporting Information is available from the Wiley Online Library or from the author.

Acknowledgements

A part of this work was financially supported by a research project, "Advanced Low Carbon Technology Research and Development Program for Specially Promoted Research for Innovative Next Generation Batteries" of the Japan Science and Technology Agency (JST-ALCA SPRING, JPMJAC1301), which is gratefully acknowledged. H.Y. acknowledges Suzuki Foundation for the financial support. V.T. thanks the Natural Sciences and Engineering Research Council of Canada (NSERC) for supporting this work through discovery grants (Award number: RGPIN-2021-02493). The authors would also like to thank Mr. Keisuke Shinoda for his technical support for FIB-SEM-EDS.

Conflict of Interest

The authors declare no conflict of interest.

Data Availability Statement

The data that support the findings of this study are available from the corresponding author upon reasonable request.

Keywords

all-solid-state batteries, garnet-type lithium-ion conductors, pressure-less processes, quick liquid phase sintering, solid electrolytes

Received: March 5, 2023
Revised: March 26, 2023
Published online:

[1] K. Takada, *Acta Mater.* **2013**, *61*, 759.
[2] V. Thangadurai, B. Chen, *Chem. Mater.* **2022**, *34*, 6637.
[3] Y. Iriyama, M. Wadaguchi, K. Yoshida, Y. Yamamoto, M. Motoyama, T. Yamamoto, *J. Power Sources* **2018**, *385*, 55.
[4] C. Yada, A. Ohmori, K. Ide, H. Yamasaki, T. Kato, T. Saito, F. Sagane, Y. Iriyama, *Adv. Energy Mater.* **2014**, *4*, 1301416.
[5] R. Murugan, V. Thangadurai, W. Weppner, *Angew. Chem., Int. Ed.* **2007**, *46*, 7778.
[6] C. Wang, K. Fu, S. P. Kammampata, D. W. McOwen, A. J. Samson, L. Zhang, G. T. Hitz, A. M. Nolan, E. D. Wachsman, Y. Mo, V. Thangadurai, L. Hu, *Chem. Rev.* **2020**, *120*, 4257.
[7] A. J. Samson, K. Hofstetter, S. Bag, V. Thangadurai, *Energy Environ. Sci.* **2019**, *12*, 2957.
[8] S. Ohta, T. Kobayashi, J. Seki, T. Asaoka, *J. Power Sources* **2012**, *202*, 332.
[9] R. Sudo, Y. Nakata, K. Ishiguro, M. Matsui, A. Hirano, Y. Takeda, O. Yamamoto, N. Imanishi, *Solid State Ionics* **2014**, *262*, 151.
[10] L. Cheng, C. H. Wu, A. Jarry, W. Chen, Y. Ye, J. Zhu, R. Kostecki, K. Persson, J. Guo, M. Salmeron, G. Chen, M. Doeff, *ACS Appl. Mater. Interfaces* **2015**, *7*, 17649.
[11] C.-L. Tsai, V. Roddatis, C. V. Chandran, Q. Ma, S. Uhlenbruck, M. Bram, P. Heitjans, O. Guillon, *ACS Appl. Mater. Interfaces* **2016**, *8*, 10617.
[12] A. Sharafi, H. M. Meyer, J. Nanda, J. Wolfenstine, J. Sakamoto, *J. Power Sources* **2016**, *302*, 135.
[13] K. Ishiguro, Y. Nakata, M. Matsui, I. Uechi, Y. Takeda, O. Yamamoto, N. Imanishi, *J. Electrochem. Soc.* **2013**, *160*, A1690.
[14] K. Ishiguro, H. Nemori, S. Sunahiro, Y. Nakata, R. Sudo, M. Matsui, Y. Takeda, O. Yamamoto, N. Imanishi, *J. Electrochem. Soc.* **2014**, *161*, A668.
[15] Y. Ren, Y. Shen, Y. Lin, C. W. Nan, *Electrochem. Commun.* **2015**, *57*, 27.
[16] Y. Suzuki, K. Kami, K. Watanabe, A. Watanabe, N. Saito, T. Ohnishi, K. Takada, R. Sudo, N. Imanishi, *Solid State Ionics* **2015**, *278*, 172.
[17] L. Cheng, W. Chen, M. Kunz, K. Persson, N. Tamura, G. Chen, M. Doeff, *ACS Appl. Mater. Interfaces* **2015**, *7*, 2073.
[18] N. J. Taylor, S. Stangeland-Molo, C. G. Haslam, A. Sharafi, T. Thompson, M. Wang, R. Garcia-Mendez, J. Sakamoto, *J. Power Sources* **2018**, *396*, 314.
[19] Y. Kim, A. Yoo, R. Schmidt, A. Sharafi, H. Lee, J. Wolfenstine, J. Sakamoto, *Front. Energy Res.* **2016**, *4*, 20.
[20] H. Yamada, T. Ito, R. H. Basappa, *Electrochim. Acta* **2016**, *222*, 648.
[21] R. H. Basappa, T. Ito, H. Yamada, *J. Electrochem. Soc.* **2017**, *164*, A666.
[22] E. J. Cheng, A. Sharafi, J. Sakamoto, *Electrochim. Acta* **2017**, *223*, 85.
[23] L. Porz, T. Swamy, B. W. Sheldon, D. Rettenwander, T. Frömling, S. Berendts, R. Uecker, W. C. Carter, Y. Chiang, *Adv. Energy Mater.* **2017**, *7*, 1701003.
[24] A. Sharafi, E. Kazyak, A. L. Davis, S. Yu, T. Thompson, D. J. Siegel, N. P. Dasgupta, J. Sakamoto, *Chem. Mater.* **2017**, *29*, 7961.
[25] S. Sarkar, B. Chen, C. Zhou, S. N. Shirazi, F. Langer, J. Schwenzel, V. Thangadurai, *Adv. Energy Mater.* **2023**, *13*, 2203897.
[26] S. Sarkar, V. Thangadurai, *ACS Energy Lett.* **2022**, *7*, 1492.
[27] Y. Kobayashi, T. Takeuchi, M. Tabuchi, K. Ado, H. Kageyama, *J. Power Sources* **1999**, *81-82*, 853.
[28] K. H. Kim, Y. Iriyama, K. Yamamoto, S. Kumazaki, T. Asaka, K. Tanabe, C. A. J. Fisher, T. Hirayama, R. Murugan, Z. Ogumi, *J. Power Sources* **2011**, *196*, 764.
[29] G. Vardar, W. J. Bowman, Q. Lu, J. Wang, R. J. Chater, A. Aguadero, R. Seibert, J. Terry, A. Hunt, I. Waluyo, D. D. Fong, A. Jarry, E. J. Crumlin, S. L. Hellstrom, Y. M. Chiang, B. Yildiz, *Chem. Mater.* **2018**, *30*, 6259.
[30] S. Ohta, S. Komagata, J. Seki, T. Saeki, S. Morishita, T. Asaoka, *J. Power Sources* **2013**, *238*, 53.
[31] K. Nagao, A. Hayashi, M. Tatsumisago, *J. Ceram. Soc. Jpn.* **2016**, *124*, 915.
[32] F. Han, J. Yue, C. Chen, N. Zhao, X. Fan, Z. Ma, T. Gao, F. Wang, X. Guo, C. Wang, *Joule* **2018**, *2*, 497.
[33] S. Uhlenbruck, J. Dornseiffer, S. Lobe, C. Dellen, C.-L. L. Tsai, B. Gotzen, D. Sebold, M. Finsterbusch, O. Guillon, *J. Electroceramics* **2017**, *38*, 197.
[34] C.-L. Tsai, Q. Ma, C. Dellen, S. Lobe, F. Vondahlen, A. Windmüller, D. Grüner, H. Zheng, S. Uhlenbruck, M. Finsterbusch, F. Tietz, D. Fattakhova-Rohlfing, H. P. Buchkremer, O. Guillon, *Sustainable Energy Fuels* **2019**, *3*, 280.
[35] M. Ihrig, M. Finsterbusch, C. L. Tsai, A. M. Laptev, C. hao Tu, M. Bram, Y. J. Sohn, R. Ye, S. Sevinc, S. kang Lin, D. Fattakhova-Rohlfing, O. Guillon, *J. Power Sources* **2021**, *482*, 228905.

[36] S. Ohta, M. Kawakami, H. Nozaki, C. Yada, T. Saito, H. Iba, *J. Mater. Chem. A* **2020**, *8*, 8989.
[37] H. Yamada, T. Ito, R. H. Basappa, R. Bekarevich, K. Mitsuishi, *J. Power Sources* **2017**, *368*, 97.
[38] K. Sato, K. Suzuki, R. Narumi, K. Yashiro, T. Hashida, J. Mizusaki, *Jpn. J. Appl. Phys.* **2011**, *50*, 055803.
[39] W. Araki, Y. Imai, T. Adachi, *J. Eur. Ceram. Soc.* **2009**, *29*, 2275.
[40] R. M. German, P. Suri, S. J. Park, *J. Mater. Sci.* **2009**, *44*, 1.
[41] K. Tadanaga, R. Takano, T. Ichinose, S. Mori, A. Hayashi, M. Tatsumisago, *Electrochem. Commun.* **2013**, *33*, 51.
[42] N. C. Rosero-Navarro, T. Yamashita, A. Miura, M. Higuchi, K. Tadanaga, *J. Am. Ceram. Soc.* **2017**, *100*, 276.
[43] N. C. Rosero-Navarro, T. Yamashita, A. Miura, M. Higuchi, K. Tadanaga, *Solid State Ionics* **2016**, *285*, 6.
[44] X. Xiao, H. Wagata, F. Hayashi, H. Onodera, K. Yubuta, N. Zettsu, S. Oishi, K. Teshima, *Cryst. Growth Des.* **2015**, *15*, 4863.
[45] Y. Mizuno, N. Zettsu, K. Yubuta, T. Sakaguchi, T. Saito, H. Wagata, S. Oishi, K. Teshima, *Cryst. Growth Des.* **2014**, *14*, 1882.
[46] P. Albertus, V. Anandan, C. Ban, N. Balsara, I. Belharouak, J. Buettner-Garrett, Z. Chen, C. Daniel, M. Doeff, N. J. Dudney, B. Dunn, S. J. Harris, S. Herle, E. Herbert, S. Kalnaus, J. A. Libera, D. Lu, S. Martin, B. D. McCloskey, M. T. McDowell, Y. S. Meng, J. Nanda, J. Sakamoto, E. C. Self, S. Tepavcevic, E. Wachsman, C. Wang, A. S. Westover, J. Xiao, T. Yersak, *ACS Energy Lett.* **2021**, *6*, 1399.
[47] Y. Ren, T. Danner, A. Moy, M. Finsterbusch, T. Hamann, J. Dippell, T. Fuchs, M. Müller, R. Hoft, A. Weber, L. A. Curtiss, P. Zapol, M. Klenk, A. T. Ngo, P. Barai, B. C. Wood, R. Shi, L. F. Wan, T. W. Heo, M. Engels, J. Nanda, F. H. Richter, A. Latz, V. Srinivasan, J. Janek, J. Sakamoto, E. D. Wachsman, D. Fattakhova-Rohlfing, *Adv. Energy Mater.* **2022**, *13*, 2201939.
[48] S. Abou-Warda, W. Pietzuch, G. Berghöfer, U. Kesper, W. Massa, D. Reinen, *J. Solid State Chem.* **1998**, *138*, 18.
[49] H. Yamada, T. Ito, S. P. Kammampata, V. Thangadurai, P. Kammampata, V. Thangadurai, S. P. Kammampata, V. Thangadurai, *ACS Appl. Mater. Interfaces* **2020**, *12*, 36119.
[50] S. P. Kammampata, R. H. Basappa, T. Ito, H. Yamada, V. Thangadurai, *ACS Appl. Energy Mater.* **2019**, *2*, 1765.
[51] K. W. Schneider, C. A. Rasband, W. S. Eliceiri, *Nat. Methods* **2012**, *9*, 671.
[52] G. G. Amatucci, J. M. Tarascon, L. C. Klein, *J. Electrochem. Soc.* **1996**, *143*, 1114.
[53] M. Fakkao, Y. Kimura, K. Funayama, T. Nakamura, N. Kuwata, J. Kawamura, T. Kawada, K. Amezawa, *Solid State Ionics* **2017**, *299*, 8.
[54] K. Ariyoshi, K. Yuzawa, Y. Yamada, *J. Phys. Chem. C* **2020**, *124*, 8170.
[55] K. J. Kim, J. L. M. Rupp, *Energy Environ. Sci.* **2020**, *13*, 4930.
[56] N. Hayashi, K. Watanabe, K. Shimanoe, *J. Mater. Chem. A* **2023**, *11*, 2042.
[57] M. Okubo, Y. Tanaka, H. Zhou, T. Kudo, I. Honma, *J. Phys. Chem. B* **2009**, *113*, 2840.
[58] K. Nakamura, M. Yamamoto, K. Okamura, Y. Michihiro, I. Nakabayashi, T. Kanashiro, **1999**, *121*, 301.
[59] K. Nakamura, H. Ohno, K. Okamura, Y. Michihiro, T. Moriga, I. Nakabayashi, T. Kanashiro, *Solid State Ionics* **2006**, *177*, 821.
[60] G. Hasegawa, N. Kuwata, Y. Tanaka, T. Miyazaki, N. Ishigaki, K. Takada, J. Kawamura, *Phys. Chem. Chem. Phys.* **2020**, *23*, 2438.
[61] M. Ihrig, M. Finsterbusch, A. M. Laptev, C. Tu, N. T. T. Tran, C. Lin, L.-Y. Kuo, R. Ye, Y. J. Sohn, P. Kaghazchi, S. Lin, D. Fattakhova-Rohlfing, O. Guillon, *ACS Appl. Mater. Interfaces* **2022**, *14*, 11288.
[62] M. Ihrig, L.-Y. Kuo, S. Lobe, A. M. Laptev, C. Lin, C. Tu, R. Ye, P. Kaghazchi, L. Cressa, S. Eswara, S. Lin, O. Guillon, D. Fattakhova-Rohlfing, M. Finsterbusch, *ACS Appl. Mater. Interfaces* **2023**, *15*, 4101.
[63] A. Sakuda, A. Hayashi, M. Tatsumisago, *Chem. Mater.* **2010**, *22*, 949.
[64] C. Tsai, Q. Ma, C. Dellen, S. Lobe, F. Vondahlen, A. Windmüller, D. Grüner, H. Zheng, S. Uhlenbruch, M. Finsterbusch, F. Tietz, D. Fattakhova-Rohlfing, H. P. Buchkremer, O. Guillon, *Sustainable Energy Fuels* **2018**, *3*, 280.
[65] E. J. Cheng, N. J. Taylor, J. Wolfenstine, J. Sakamoto, *J. Asian Ceram. Soc.* **2017**, *5*, 113.
[66] X. Lu, A. Bertei, D. P. Finegan, C. Tan, S. R. Daemi, J. S. Weaving, K. B. O'Regan, T. M. M. Heenan, G. Hinds, E. Kendrick, D. J. L. Brett, P. R. Shearing, *Nat. Commun.* **2020**, *11*, 2079.
[67] J. Scharf, M. Chouchane, D. P. Finegan, B. Lu, C. Redquest, M. Kim, W. Yao, A. A. Franco, D. Gostovic, Z. Liu, M. Riccio, F. Zelenka, J. M. Doux, Y. S. Meng, *Nat. Nanotechnol.* **2022**, *17*, 446.
[68] M. Ihrig, R. Ye, A. M. Laptev, D. Grüner, R. Guerdelli, W.-S. Scheld, M. Finsterbusch, H.-D. Wiemhöfer, D. Fattakhova-Rohlfing, O. Guillon, *ACS Appl. Energy Mater.* **2021**, *4*, 10428.
[69] T. Ohzuku, A. Ueda, N. Yamamota, *J. Electrochem. Soc.* **1995**, *142*, 1431.
[70] K. Ariyoshi, H. Yamamoto, Y. Yamada, *Electrochim. Acta* **2018**, *260*, 498.
[71] F. Strauss, L. De Biasi, A. Y. Kim, J. Hertle, S. Schweidler, J. Janek, P. Hartmann, T. Brezesinski, *ACS Mater. Lett.* **2020**, *2*, 84.
[72] S. P. Kammampata, H. Yamada, T. Ito, R. Paul, V. Thangadurai, *J. Mater. Chem. A* **2020**, *8*, 2581.
[73] R. H. Basappa, T. Ito, T. Morimura, R. Bekarevich, K. Mitsuishi, H. Yamada, *J. Power Sources* **2017**, *363*, 145.